Computer simulations of hard pear-shaped particles

F. Barmes[1,2], M. Ricci[2], C. Zannoni[2] and D.J. Cleaver[1]

[1]Materials Research Institute
Sheffield Hallam University
Sheffield
S1 1WB
United Kingdom

[2]Dip.di Chimica Fisica ed Inorganica
Università di Bologna
40136 Bologna
Italy

June 4, 2003

1

Abstract

We report results obtained from Monte Carlo simulations investigating mesophase formation in two model systems of hard pear-shaped particles. The first model considered is a hard variant of the truncated Stone-Expansion model previously shown to form nematic and smectic mesophases when embedded within a 12-6 Gay-Berne-like potential [1]. When stripped of its attractive interactions, however, this system is found to lose its liquid crystalline phases. For particles of length to breadth ratio $k = 3$, glassy behaviour is seen at high pressures, whereas for $k = 5$ several bi-layer-like domains are seen, with high intradomain order but little interdomain orientational correlation. For the second model, which uses a parametric shape parameter based on the generalised Gay-Berne formalism, results are presented for particles with elongation $k = 3, 4$ and 5. Here, the systems with $k = 3$ and 4 fail to display orientationally ordered phases, but that with $k = 5$ shows isotropic, nematic and, unusually for a hard-particle model, interdigitated smectic A_2 phases.

1 Introduction

In recent years, flexoelectricity has become an increasingly important feature in the design of materials for use in liquid crystal devices. Flexoelectric behaviour, which leads to field-induced director distortion, results, at a molecular level, from competition between electric and steric dipolar interactions. As well as leading to modified bulk properties, flexoelectricity has been mooted to be a possible driver for switching in devices with bistable anchoring surfaces [2]. Indeed, it has been suggested that the switching mechanism of the zenithally bistable device [3] may rely, in part, on flexoelectric behaviour.

The early studies of Meyer [4] and Prost and Marcerou [5], showed that the mechanisms underlying flexoelectricity can be understood in two ways. In the original explanation from Meyer, flexoelectric behavior was explained in terms of particles with a strong anisotropy in their charge repartition. Thus, it was shown that, upon polarization by an applied field, pear-shaped particles exhibit a splay director distortion, whereas banana-shaped particles exhibit a bend distortion. Subsequently, Prost and Marcerou showed that flexoelectricity could also be obtained using particles with a non-zero quadrupole moment. This did not contradict Meyer's original work, however, since in reality flexoelectric mesogens are known to possess either one or both of these properties [6].

Although well studied theoretically [7–9], few computer simulations using flexoelectric particles have been performed to date. Whilst particle based simulations showing ferroelectric behaviour are reasonably well established (see, *e.g.*, [10, 11]), models with the dipolar and/or quadrupolar symmetry

steric interactions needed for flexoelectric behaviour are relatively scarce.

Neal and co-workers performed one such study using molecules represented by rigid assemblies of three Gay-Berne sites [12]. One of the assemblies considered in Ref. [12] was a triangular arrangement of mutually parallel Gay-Berne sites, leading, overall, to approximately pear-shaped molecules. On compression, a system of such molecules ordered from an isotropic liquid to a smectic arrangement in which the molecular orientations in successive layers were almost perfectly anti-parallel. Subsequently, Stelzer *et al.* [13] investigated the behaviour of pear-shaped molecules using a model with two interaction sites per particle; each particle comprised a Lennard-Jones site embedded near to one end of a Gay-Berne site. Isotropic, nematic and smectic phases were observed, local antiparallel alignment being seen in the nematic phase. Measurements of the splay and bend flexoelectric coefficients gave a non-zero splay coefficient and, to within error estimates, a zero bend coefficient in accordance with Meyer's theory. Equivalent simulations by Billeter and Pelcovits [14], using qualitatively the same model but with different energy parametrisations and an alternative method for the calculation of the flexoelectric coefficients, confirmed the results of Ref. [13]. In this case, however, no stable nematic phase was found between the isotropic and (locally antiparallel) smectic A phases.

Whilst the results from these systems proved encouraging, their reliance on multi-site generic potentials remained a relative inefficiency. This was resolved somewhat in recent work by Berardi and some of the current authors [1], in which a single-site model was developed, using Zewdie's generalisation approach [15, 16], to represent tapered or pear-shaped particles. Here, using the geometrical shape of a Bézier curve as a template for the

particle shape, a numerically calculated mesh of contact distance values was fitted using a truncated Stone expansion which, in turn, was employed in the simulations themselves. Results from this study were very encouraging, as both nematic and smectic A phases were found, and, through appropriate manipulation of the well-depth anisotropy terms, equivalent phases with net *polar* order were generated.

In this paper, we seek to explore the fundamental properties of single-site pear-shaped models such as that used in Ref [1], by investigating mesophase formation in systems of hard, noncentrosymmetric particles. Hard particle simulations have proved to be an effective and efficient testbed for many of the theories of liquid crystal physics [17], and have confirmed that shape anisotropy alone can be sufficient for the onset of nematic and even smectic order. Two distinct systems are described here. The first is a hard version of the truncated Stone expansion potential described in [1]. The second employs a novel approach, based on a parametric variant of the generalized Gay-Berne shape parameter [18], which yields an analytical expression for the contact distance between two pear-shaped objects.

The content of the remainder of this paper is arranged as follows. In subsection 2.1 we give a brief description of the truncated Stone expansion potential before presenting and discussing results obtained from Monte Carlo simulations of same. In the following subsection, we introduce the parametric approach for generating shape parameters for non-ellipsoidal particles, and apply it to generate shape parameters for the Bézier pears considered in Ref. [1]. Results obtained from Monte Carlo simulations of such systems are presented in subsection 2.2.3. Finally, the two sets of simulations are compared and discussed in Section 3.

2 Simulations of hard pears.

2.1 The truncated Stone expansion model

2.1.1 Model Details

Our first simulations of hard pear-shaped particles used a steric version of the potential described in Ref. [1]. This gives the interaction between two particles, i and j, as

$$\mathcal{V}^{HP} = \begin{cases} \infty & \text{if} \quad r_{ij} < \sigma(\hat{\mathbf{u}}_i, \hat{\mathbf{u}}_j, \hat{\mathbf{r}}_{ij}) \\ 0 & \text{if} \quad r_{ij} \geq \sigma(\hat{\mathbf{u}}_i, \hat{\mathbf{u}}_j, \hat{\mathbf{r}}_{ij}) \end{cases} \tag{1}$$

where $\sigma(\hat{\mathbf{u}}_i, \hat{\mathbf{u}}_j, \hat{\mathbf{r}}_{ij})$ represents the contact distance between two pear-shaped particles with orientations $\hat{\mathbf{u}}_i$ and $\hat{\mathbf{u}}_j$ and $\hat{\mathbf{r}}_{ij} = \frac{\mathbf{r}_{ij}}{r_{ij}}$ and $\mathbf{r}_{ij}$ is the intermolecular vector. Following the approach of Zewdie [15, 16], this contact distance was expressed as an expansion of the form

$$\begin{aligned} \sigma(\hat{\mathbf{u}}_i, \hat{\mathbf{u}}_j, \hat{\mathbf{r}}_{ij}) &\simeq \mathcal{L}(\hat{\mathbf{u}}_i, \hat{\mathbf{u}}_j, \hat{\mathbf{r}}_{ij}) \\ &= \sum_{L_1, L_2, L_3} \sigma_{L_1, L_2, L_3} S^{*L_1, L_2, L_3}(\hat{\mathbf{u}}_i, \hat{\mathbf{u}}_j, \hat{\mathbf{r}}_{ij}) \end{aligned} \tag{2}$$

where S^{L_1, L_2, L_3} is a Stone function [19], and the expansion coefficients σ_{L_1, L_2, L_3} are given by

$$\sigma_{L_1, L_2, L_3} = \frac{\int \mathcal{L}(\hat{\mathbf{u}}_i, \hat{\mathbf{u}}_j, \hat{\mathbf{r}}_{ij}) S^{L_1, L_2, L_3}(\hat{\mathbf{u}}_i, \hat{\mathbf{u}}_j, \hat{\mathbf{r}}_{ij}) d\hat{\mathbf{u}}_i d\hat{\mathbf{u}}_j d\hat{\mathbf{r}}_{ij}}{\int S^{*L_1, L_2, L_3}(\hat{\mathbf{u}}_i, \hat{\mathbf{u}}_j, \hat{\mathbf{r}}_{ij}) S^{L_1, L_2, L_3}(\hat{\mathbf{u}}_i, \hat{\mathbf{u}}_j, \hat{\mathbf{r}}_{ij}) d\hat{\mathbf{u}}_i d\hat{\mathbf{u}}_j d\hat{\mathbf{r}}_{ij}}. \tag{3}$$

Simulations were performed with two parameterisations of this model, with length to breadth ratios, k, of 3 and 5 respectively. In both cases the shape parameter expansion (2) was restricted to indices $\{L_1, L_2, L_3\} = 1 \ldots 6$; the expansion coefficients used for $k = 3$ were identical to those given in Ref. [1], while those for $k = 5$ are listed in Table 1.

2.1.2 Simulation Results

Our first simulations were performed on a system of 1250 particles with elongation $k = 3$ using constant NPT Monte Carlo (MC) techniques. This system was chosen since it was shown in Ref. [1] that the attractive version of this model with elongation $k = 3$ has isotropic, nematic and smectic phases. In addition to the normal positional and orientational MC moves, one fifth of the attempted particle moves were orientation inversions, implemented through the reversal of the appropriate $\hat{\mathbf{u}}_i$ vector. Volume change moves were attempted, on average, once every two MC sweeps, where one sweep represents one attempted move per particle in the system. Within these volume change moves, each box dimension was allowed to change independently so as to minimise the influence of the periodic boundary conditions during the formation of possible smectic phases [20]. Typically, run lengths of 0.5 to 1×10^6 MC sweeps were used for equilibration and production phases, but at the highest densities considered, equilibration runs were extended up to 5×10^6 MC sweeps. Two separate simulation sequences were performed. The first was a compression sequence starting from a low density phase with a fully isotropic initial distribution of particle orientations. The second was an expansion sequence, the starting configuration for which was generated by taking a high density configuration obtained from the compression sequence and inducing the particle orientations to align with the $(0, 0, 1)$ direction. This was achieved by applying a uniform field with this orientation to the system and assuming a strong molecular coupling via a positive dielectric anisotropy.

The equation of state and nematic, $< P_2 >$, and polar, $< P_1 >$ order parameter data [21] obtained from these simulations are shown in Fig. 1a.

Surprisingly, the results obtained from the compression sequence show no spontaneous ordering, and at all densities $< P_2 >$ falls short of the values typical of a nematic phase. In contrast, the expansion sequence (with a field-aligned initial configuration) performed on this system has some reasonably high $< P_2 >$ values, consistent with nematic order being present at the higher densities considered. The discrepancy between these two sets of order parameter values is also seen in the equation of state data and indicates a failure of this system to equilibrate at densities $\rho^* > 0.30$. We return to the causes of this non-equilibration below.

An equivalent compression sequence was performed using a system of 1000 particles with elongation $k = 5$. This system was studied since increasing particle shape anisotropy generally promotes mesophase formation. While the equation of state data obtained for this system showed a slight inflection and $< P_2 >$ attained values of 0.3 (Fig. 1b), the behaviour expected for an isotropic-nematic transition was again absent. Configuration snapshots from high density runs performed using this system (*e.g.* Fig. 2) showed that the modest order parameter values resulted from the formation of numerous bi-layer-like domains. While the local order within these domains was very high, orientational correlations between the domains were weak. This multi-domain structure persisted even when run-lengths were extended significantly.

The failure of these hard-particle systems to reproduce the density-driven nematic-isotropic transition shown by the equivalent soft particle model is a surprising result; by contrast, the nematic-isotropic transition densities of hard gaussian overlap model [22] are virtually identical to those of the equivalent (soft) Gay-Berne systems [23, 24]. Indeed, the failure of our hard

8

pear systems to form nematic phases could be taken as an indication that particle shape did not contribute significantly to the mesophase formation processes seen in Ref. [1]. To assess both this and the non-equilibration noted above, we have measured the particle mobility in our systems by computing the mean square displacement

$$\langle \delta r^2(n) \rangle = \langle (\mathbf{r}_n - \mathbf{r}_0)^2 \rangle \tag{4}$$

where $\mathbf{r}_n - \mathbf{r}_0$ is the displacement vector moved by a particle in n consecutive MC sweeps and the angled brackets indicate an average over all particles and the run length. In MC simulations with fixed maximum particle displacement, Brownian diffusion dictates that $\langle \delta r^2(n) \rangle$ should increase linearly with n in a fluid phase. Instead, the $\langle \delta r^2(n) \rangle$ data for $k = 3$ (fig 3a), show that, as the density was increased, the mobility of the particles decreased dramatically, indicating the onset of glassy behaviour. This observation is certainly consistent with our earlier conclusion that equilibration was not achieved at high densities; for both of our simulation sequences for $k = 3$, the sampling of configuration space will have been poor for $\rho^* \geq 0.30$. For the $k = 5$ system, the measured mobility again showed a marked decrease with increase in density, although it did not reach the very low levels found at $k = 3$ (fig 3b). We note, however, that $\langle \delta r^2(n) \rangle$ does not distinguish between single particle diffusion and en-masse mobility of larger assemblies such as the bilayer domains seen in Fig. 2.

The low mobilities found at high densities in these systems can be explained by consideration of details of the shape parameters obtained by truncating the expansion (2) at $\{L_1, L_2, L_3\} = 1 \ldots 6$. To illustrate this, we show, in Figs. 4, sample shape parameters for parallel and anti-parallel particle configurations (i.e. $(\mathbf{u_i} \cdot \mathbf{u_j}) = -1$ and 1) for both $k = 3$ and $k = 5$. These reveal

9

that the contact functions used in our simulations were not purely convex, as had been supposed, but had significant ridges. We suggest that in our $k = 3$ simulations, these non-convex features were sufficient to prevent particles from sliding past one another and so gave rise to locked configurations. For the $k = 5$ particles, for which strong local ordering was achieved, we note that the shape parameter for antiparallel particles (illustrated in Fig. 4d) has an equatorial ridge which presumably leads to the interlocked bilayer structures so prevalent in Fig. 2.

These problems are similar to those encountered in Ref. [25] where simulations were performed using a seven site linear hard sphere chain (LHSC) model. This model was found to form metastable glassy states in the vicinity of the isotropic-nematic transition due to the non-convex shapes of the particles which inhibited their ability to slide past one another. The tendency of these systems to become irretrievably interlocked was overcome in Ref. [25] by the use of reptation moves. This solution was not available to us here, however, since ours is a single-site model.

Once in a stable nematic phase, the LHSC model proved to be reasonably well behaved, exhibiting a stable nematic region and undergoing a reversible nematic-smectic A transition. This raises the question of whether the glassy behaviour we have observed here is simply a simulation bottleneck associated with the isotropic-nematic transition or a genuine pre-empting of the nematic phase by a glass. While we are not in a position to give a categorical answer to this question, the evidence we do have suggests the latter to be the case. All of our $k = 3$ simulations with $\rho^* > 0.30$ (*i.e.* those in both the compression *and* expansion sequences) had low particle mobilities, the effective diffusion coefficient decreasing monotonically with increase in applied pressure. This indicates that if there is a region of fluid, nematic phase-stability,

it lies beyond the pressure values considered here; we have certainly found no evidence that the nematic phase seen in Ref. [1] is preserved when the $k = 3$ model is stripped of its attractive interactions. From this change of phase behaviour, we infer that, for this system, the presence of attractive interactions affects the local packing of the particles – the attractive wells, being located at $r > \sigma(\hat{\mathbf{u}}_i, \hat{\mathbf{u}}_j, \hat{\mathbf{r}}_{ij})$, provide a means by which the particles can escape from the inter-locked arrangements that dominate the equivalent hard particle system at high densities. We are not aware of any other model system for which both shape anisotropy *and* attractive interactions are required to promote a nematic-isotropic transition. For the $k = 5$ hard particle system, while the measured mobility did decrease with increase in density, it did not drop as far as that found at $k = 3$. That said, the tendency of this system to form local bilayer-like packing arrangements is in conflict with the usual mechanisms of nematic phase formation (*e.g.* diverging orientational correlations), leading us to conclude that here, too, the nematic phase is probably never stable.

Faced with this unexpected phase behaviour, we present, in the following subsection, an alternative, parametric approach to developing non-centrosymmetric single-site models. By applying this approach to the Bézier pears used as a basis for the truncated Stone expansion models used in this subsection, we then derive a series of pear-shaped models for different particle elongations and perform MC simulations to investigate their ability to form mesophases.

11

2.2 The parametric hard gaussian overlap model

2.2.1 Computation of the contact distance

We start with the generalised expression for the shape parameter which governs the interaction between a pair of uniaxial, but non-identical, ellipsoidal gaussians [18]. This expression, which itself is an approximation to the hard ellipsoid contact function for non-identical ellipsoids [26], gives the contact distance between particles i and j of elongations l_i, l_j and breadths d_i, d_j as

$$\sigma(\hat{\mathbf{u}}_i, \hat{\mathbf{u}}_j, \hat{\mathbf{r}}_{ij}) = \sigma_0 \left[1 - \chi \left\{ \frac{\alpha^2 \left(\hat{\mathbf{r}}_{ij} \cdot \hat{\mathbf{u}}_i \right)^2 + \alpha^{-2} \left(\hat{\mathbf{r}}_{ij} \cdot \hat{\mathbf{u}}_j \right) - 2\chi \left(\hat{\mathbf{r}}_{ij} \cdot \hat{\mathbf{u}}_i \right) \left(\hat{\mathbf{r}}_{ij} \cdot \hat{\mathbf{u}}_j \right) \left(\hat{\mathbf{u}}_i \cdot \hat{\mathbf{u}}_j \right)}{1 - \chi^2 \left(\hat{\mathbf{u}}_i \cdot \hat{\mathbf{u}}_j \right)^2} \right\} \right]^{-\frac{1}{2}}$$

(5)

with

$$\sigma_0 = \sqrt{\frac{d_i^2 + d_j^2}{2}}$$

$$\alpha^2 = \left[\frac{(l_i^2 - d_i^2)(l_j^2 + d_i^2)}{(l_j^2 - d_j^2)(l_i^2 + d_j^2)} \right]^{\frac{1}{2}}$$

$$\chi = \left[\frac{(l_i^2 - d_i^2)(l_j^2 - d_j^2)}{(l_j^2 + d_i^2)(l_i^2 + d_j^2)} \right]^{\frac{1}{2}} .$$

If, alternatively, brackets containing the length and breadth values are grouped as

$$A = (l_i^2 - d_i^2) \quad B = (l_j^2 - d_j^2)$$
$$C = (l_j^2 + d_i^2) \quad D = (l_i^2 + d_j^2),$$

the shape parameter can be rewritten as

$$\sigma(\hat{\mathbf{u}}_i, \hat{\mathbf{u}}_j, \hat{\mathbf{r}}_{ij}) = \sigma_0 \left[1 - \frac{AC \left(\hat{\mathbf{r}}_{ij} \cdot \hat{\mathbf{u}}_i \right)^2 + BD \left(\hat{\mathbf{r}}_{ij} \cdot \hat{\mathbf{u}}_j \right)^2 - 2AB \left(\hat{\mathbf{r}}_{ij} \cdot \hat{\mathbf{u}}_i \right) \left(\hat{\mathbf{r}}_{ij} \cdot \hat{\mathbf{u}}_j \right) \left(\hat{\mathbf{u}}_i \cdot \hat{\mathbf{u}}_j \right)}{CD - AB \left(\hat{\mathbf{u}}_i \cdot \hat{\mathbf{u}}_j \right)^2} \right]^{-\frac{1}{2}} .$$

(6)

In practice, this form, being free of possible division by zero or complex numbers, is better suited for implementation in computer simulation codes.

The limitation of the expression (6) is that it is restricted to particles with ellipsoidal symmetry. The thrust of this subsection is to illustrate that, since eqn.(6) is valid for any set of particle axis lengths l_i, l_j, d_i, d_j, it can also be used for some situations in which these axis lengths, rather than being held fixed, are allowed to vary parametrically.

As an illustration of this, we consider the properties of a pear-shaped particle. When its sharp end interacts, it resembles a particle with a relatively large l/d ratio, whereas its blunt end corresponds to an l/d ratio rather nearer to unity. In generating smooth variation between these two limiting cases, a multitude of parametric forms is possible: here we restrict ourselves to making l_i and d_i simple polynomials of the polar angle $(\hat{\mathbf{r}}_{ij} \cdot \hat{\mathbf{u}}_i)$, that is

$$d_i(\hat{\mathbf{r}}_{ij} \cdot \hat{\mathbf{u}}_i) = a_{d,0} + \ldots + a_{d,n}(\hat{\mathbf{r}}_{ij} \cdot \hat{\mathbf{u}}_i)^n \tag{7}$$

$$l_i(\hat{\mathbf{r}}_{ij} \cdot \hat{\mathbf{u}}_i) = a_{l,0} + \ldots + a_{l,m}(\hat{\mathbf{r}}_{ij} \cdot \hat{\mathbf{u}}_i)^m. \tag{8}$$

Whilst this restriction limits, to some extent, the range of particle shapes available, it has the advantage that the effect of this parametric approach on $\sigma(\hat{\mathbf{u}}_i, \hat{\mathbf{u}}_j, \hat{\mathbf{r}}_{ij})$ is transparent: through the coefficients A, B, C and D, it simply introduces higher order dependence of $\sigma(\hat{\mathbf{u}}_i, \hat{\mathbf{u}}_j, \hat{\mathbf{r}}_{ij})$ on the scalar products $(\hat{\mathbf{r}}_{ij} \cdot \hat{\mathbf{u}}_i)$ and $(\hat{\mathbf{r}}_{ij} \cdot \hat{\mathbf{u}}_j)$. On a more practical level, we note that restricting the shape parameter expansion to polynomials in these dot products has the benefit of making it readily usable in a molecular dynamics (MD) simulation. To reflect the generalisation introduced by this approach, we name the resultant class of model the parametric hard gaussian overlap (PHGO).

13

As we show in the following subsections, by working through a specific example, this parametric approach can be used to generalise the HGO model to give shape parameters which approximate other convex and axially symmetric particle shapes. We note, however, that since the PHGO's departure from the conventional HGO shape parameter is based, in part, on the interparticle vector, $\mathbf{r}_{ij}$, it ignores some possible close contacts and is *not*, therefore, suitable for modelling particles with concave surface regions (*e.g* dumbells). For systems which do satisfy the convexity criterion, however, the approximations inherent in the PHGO approach are outweighed by the advantages: it yields an analytical form for the shape parameter, making it suitable for either MC or MD simulation and is easy to embed into a Gay-Berne type model; it introduces little computational overhead, beyond that required to simulate the standard HGO model; and, since it is a simple generalisation of the HGO model, it can readily be used to represent some or all of the particles in a multi-component mixture or a multi-site model (indeed, extension to polydispersity and/or dynamic particle shape variation is quite straightforward).

2.2.2 Parameterising Bézier pears

In order to test the PHGO approach, we have used it to generate shape parameters for pear-shaped particles based on Bézier-curves (i.e. the same target system as was employed in Ref. [1]). For this, the ideal particle shape was first determined geometrically using a combination of two Bézier curves as shown in Fig. 5. This geometry is very similar to that used in Ref. [1], the exception being that we took points q_2 and q_3 to be coincident. This has the advantage of making the Bézier points' coordinates more easily scalable with

the desired length to breadth ratio k. The coordinates of the Bézier points used are given in Table 2.

From these points, it is possible to extract the coordinates of any point on the curve [27]. By taking these Bézier curves to correspond to the contact surface between a pear shaped particle i and a point probe j (*i.e.* taking $l_j = d_j = 0$ in eqn.(6)), it can readily be shown that these points need to be fitted by the particle-point shape parameter

$$\sigma(\hat{\mathbf{u}}_i, \mathbf{r}_{ij}) = \frac{d_i(\hat{\mathbf{r}}_{ij} \cdot \hat{\mathbf{u}}_i) l_i(\hat{\mathbf{r}}_{ij} \cdot \hat{\mathbf{u}}_i)}{\left[l_i^2(\hat{\mathbf{r}}_{ij} \cdot \hat{\mathbf{u}}_i) + (\hat{\mathbf{u}}_i \cdot \hat{\mathbf{r}}_{ij})^2 \left(d_i^2(\hat{\mathbf{r}}_{ij} \cdot \hat{\mathbf{u}}_i) - l_i^2(\hat{\mathbf{r}}_{ij} \cdot \hat{\mathbf{u}}_i) \right) \right]^{\frac{1}{2}}}. \qquad (9)$$

To achieve this, various polynomial forms were considered for the expansions of $d_i((\hat{\mathbf{r}}_{ij} \cdot \hat{\mathbf{u}}_i))$ and $l_i((\hat{\mathbf{r}}_{ij} \cdot \hat{\mathbf{u}}_i))$ in eqns.(8), these being fitted numerically using a simplex least squares minimisation method [28]. Good fits were obtained by taking 10 terms in the particle breadth polynomial and 2 in the length polynomial. Full sets of the coefficients obtained are given in Table 3 for particles with overall aspect ratios $k = 3$, 4 and 5.

In order to assess the accuracy of this fitting procedure, we present in Fig. 3a plot comparing the target Bézier curve and the corresponding fitted shape parameter for $k = 5$. The strong correspondence between these data sets, whilst encouraging, does not guarantee that the particle-particle potential will be as required. To assess this more fully, we computed the contact surfaces between two pears as a function of $\hat{\mathbf{r}}_{ij}$ uniformly distributed on the unit sphere. For this, the orientations $\hat{\mathbf{u}}_i$ and $\hat{\mathbf{u}}_j$ were held fixed and the three cases $\hat{\mathbf{u}}_i = \hat{\mathbf{u}}_j = (0, 0, 1)$, $\hat{\mathbf{u}}_i = -\hat{\mathbf{u}}_j = (0, 0, 1)$ and $\hat{\mathbf{u}}_i = (0, 0, 1), \hat{\mathbf{u}}_j = (0, 1, 0)$ were considered. The parallel and anti-parallel surfaces are shown for $k = 5$ in Figs. 7. As required, an approximately ellipsoidal contact surface is obtained when the two particles are parallel, and a pear shape when they

15

are anti-parallel. The orthogonal case (which is not shown since it is rather unpreposessing), is a more severe test since here the point of contact is often well away from the line of centres. We have found that this case gives an asymmetrical lobe shape which we have found to be consistent with the equivalent surface given by the models of Ref. [1]. Importantly, we note that all three of the PHGO contact functions considered in this way are almost perfectly convex, and, so, should not be prone to the locking-up suffered by the truncated Stone function expansion models simulated in subsection 2.1. In the next subsection, we go on to investigate both this assertion and the general applicability of our parametric models to molecular simulation by performing constant NPT Monte Carlo compression sequences on PHGO pear systems with $k = 3$, 4 and 5.

2.2.3   Simulation Results

In order to test our models, we have examined their phase behaviour via MC simulations in the isothermal-isobaric ensemble using $N = 1000$ particles and a series of increasing pressures. Three particle elongations, $k = 3, 4$ and 5, have been studied, their phase behaviour being assessed through the variation of the number density, ρ^*, and the polar and nematic order parameters, $< P_1 >$ and $< P_2 >$, respectively. The volume change scheme used here was the same as that used with the Stone expansion model and typical run lengths were 0.5×10^6 to 1×10^6 for equilibration and production.

The improved equilibration behaviour of these systems meant that the very long runs used previously were unnecessary here. The results of these simulations are illustrated by the plots presented in Figs. 8. For the sake of brevity,

16

results for $k = 3$ system are not shown here since they are qualitatively the same as those found for $k = 4$.

The behaviour of the order parameters for the two lower values of k indicates that there was no long range orientational ordering for these systems. $< P_1 >$ remained nearly constant at around 0.0 while $< P_2 >$ failed to reach the values (> 0.6) characteristic of nematic order. However, for both elongations, $P(\rho^*)$ had an inflection suggesting proximity to a weak phase transition. These features coincided, approximately, with the broad maxima seen in the corresponding $< P_2 >$ curves. This suggests that even if no nematic phase is shown by these systems, some other high density phase may have been formed here. We note that for these systems the particle mobilities, monitored via their mean square displacements, changed little throughout the density range considered in these simulations.

More insight into the high density arrangements adopted by these systems has been obtained through computation of the pair correlation functions resolved parallel ($g_\parallel^{\text{mol}}(r_\parallel)$) and perpendicular ($g_\perp^{\text{mol}}(r_\perp)$) to the particle orientations $\hat{\mathbf{u}}_i$ (the superscript mol is used to indicate that molecular, rather than director orientations were used to calculate these functions). These are shown in Fig. 9 for $k = 4$, and indicate local smectic-like arrangements with anti-parallel alignment of nearest neighbours within layers. However, the decay of the oscillations in $g_\parallel^{\text{mol}}(r_\parallel)$, coupled with the low corresponding $< P_2 >$ values, indicate the absence of long-ranged smectic order. Configurations snapshots illustrate these structures more clearly. As can be seen from Fig.11, with $k = 4$, upon compression, these systems formed convoluted, space filling bilayer structures, the bilayers being planar in some regions and highly curved in others. The presence of these curved regions makes these

17

systems qualitatively different from those seen in the $k = 5$ truncated Stone expansion model (recall Fig 2), where the orientations of the bilayer domains changed discontinuously with position.

For the $k = 5$ PHGO pear model, a very different situation was found. While $< P_1 >$ remained resolutely at zero for all densities, confirming an absence of polar order, $< P_2 >$ showed the well known 'S' shape characteristic of an isotropic-nematic transition and reached the values expected for an orientationally ordered phase. A corresponding plateau in the $P(\rho^*)$ curve and a configuration snapshot (Fig. 12) confirm this assessment. At higher densities, secondary features are apparent in both $P_2(\rho^*)$ and $P(\rho^*)$ indicating the presence of a second phase transition. The nature of this third phase was determined by computation of the pair correlation functions resolved parallel $(g_{\parallel}(r_{\parallel}))$ and perpendicular $(g_{\perp}(r_{\perp}))$ to the director $\hat{\mathbf{n}}$ as shown in Figs. 10(a) and (b). These graphs show that for pressures above that of the second phase transition, $g_{\parallel}(r_{\parallel})$ became periodic, indicating the onset of a smectic phase. Moreover, the decay of the oscillations in $g_{\perp}(r_{\perp})$ further indicates this to be a smectic A. A snapshot configuration from this high density region confirms this identification, a highly interdigitated bilayer smectic A_2 phase being seen, in which the molecules in adjacent layers are almost perfectly anti-parallel. This anti-parallel arrangement is apparent from the peak splitting observed in $g_{\parallel}(r_{\parallel})$, the short peaks corresponding to the distinct natural separations of particles in the two possible anti-parallel arrangements. Similar behaviour has been observed in simulations of Gay-Berne systems with longitudinal terminal molecular dipoles [29]. Comparison of the $g_{\parallel}(r_{\parallel})$ and $g_{\perp}(r_{\perp})$ data obtained at different pressures in the range $P = [2.4 : 3.8]$, shows an interesting compressibility behaviour. Upon increasing the pressure in this range, the system density rises and intra-layer particle separations decrease

slightly but the bilayer separations increase (Figs. 10(a) and (b)). From the measured $g_\parallel(r_\parallel)$ data it is found that the distance between the main peaks, which corresponds to the separation of the bilayers, increases from 7.38 to 7.66. The distance from the main peak to the first minor peak, which corresponds to the strongly interdigitating 'tail-tail' configuration increases from 2.49 to 2.76, whereas that to the second minor peak, corresponding to the weakly interdigitating 'head-head' alignment remains effectively constant at 4.85. Thus, the in-plane compression induced by this increase in pressure leads to a 10% increase in the separation within the interdigitated bilayers that comprise the smectic A_2 phase.

3 Discussion and Conclusions

In this paper, we have investigated the mesogenic behaviour of two classes of model hard pear-shaped particles, both based on a target shape built using a Bézier curve. The first model considered used a truncated Stone expansion approach to generate the particle-particle contact distance numerically. Although the Gay-Berne version of this model was well behaved, giving nematic and smectic A mesophases [1], these were *not* found on removal of the attractive interactions. Rather, the non-convex regions of the contact surfaces induced the particles to interlock, leading to the formation of multi-domain and glassy phases. For this model, therefore, it appears that the nematic-isotropic transition is not driven by particle shape alone: long-ranged orientational order is only seen when the shape is softened somewhat, by the incorporation of attractive interactions.

The second hard-pear model considered here was based on the PHGO ap-

proach, a route to non-centrosymmetric shape parameters which we have introduced in this paper. While the PHGO shape parameter is not determined from a full evaluation of the appropriate gaussian integral, the approximation it makes, that locally a non-centrosymmetric particle closely resembles an appropriately chosen ellipsoid, is intuitively reasonable. Furthermore, the computational simplicity and ready transferability of the PHGO model suggest that it may be of considerable utility in the generic modelling of self assembling systems. Here, we have found that the smooth, convex contact surfaces of a PHGO hard pear model yield stable nematic and bilayered smectic A_2 phases. Interestingly, these phases are only seen when the particle aspect ratio is increased to $k = 5$, whereas hard ellipsoid systems are know to form a nematic with k values as low as 2.75 [30]. Future work exploring the behaviour of the PHGO hard pear model will include a more thorough study of its flexoelectric properties, and an investigation into the applicability of the PHGO shape parameter in theoretical approaches commonly used to study liquid crystals.

Acknowledgements

References

[1] R.Berardi, M. Ricci and C. Zannoni. *ChemPhysChem*, 7:443, 2001.

[2] A.J. Davidson and N.J. Mottram. *Phys. Rev. E*, 65:051710, 2002.

[3] G.P. Bryan-Brown, C.V. Brown, I.C. Sage and V.C. Hui. *Nature*, 392:365, 1998.

[4] R.B. Meyer. *Phys. Rev. Letts.*, 22:918, 1969.

[5] J. Prost and J.P. Marcerou. *Le Journal de Physique*, 38:315–324, 1977.

[6] J.P. Marcerou and J. Prost. *Mol. Cryst. Liq. Cryst.*, 58:259–284, 1980.

[7] M.A. Osipov. *Sov. Phys. JETP*, 58:6, 1983.

[8] M.A. Osipov. *Le Journal de Physique Lettres*, 45:823–826, 1984.

[9] I. Dozov et al. *Le Journal de Physique Lettres*, 44:L817–L822, 1983.

[10] D. Wei and G.N. Patey. *Phys. Rev. Letts.*, 68:2043, 1992.

[11] D. Wei and G.N. Patey. *Phys. Rev. A*, 46:7783, 1992.

[12] M.P. Neal, A.J. Parker and C.M Care. *Molec. Phys.*, 91:603, 1997.

[13] J. Stelzer, R. Berardi and C. Zannoni. *Chem. Phys. Letts.*, 299:9, 1999.

[14] J.L. Billeter and R.A. Pelcovits. *Liq. Cryst.*, 27:1151, 1997.

[15] H. Zewdie. *J. Chem. Phys.*, 108:2117, 1998.

[16] H. Zewdie. *Phys. Rev. E*, 57:1793, 1998.

[17] M.P. Allen, G.T. Evans, D. Frenkel and B. Mulder. *Adv. Chem. Phys.*, 86:1, 1993.

[18] D.J. Cleaver, C.M. Care, M.P. Allen and M.P. Neal. *Phys. Rev. E*, 54:559, 1996.

[19] A.J. Stone. *Molec. Phys.*, 36:241, 1978.

[20] H. Domínguez, E. Velasco and J. Alejandre. *Molec. Phys.*, 100:2739, 2002.

[21] P. Pasini, C. Zannoni. *Advances in the computer simulations of Liquid crystals, chapter 2.* Kluwer Academic Publisher, Dordrecht, 1998.

[22] E. de Miguel, E. Martín del Río. *J. Chem. Phys.*, 115(19):90729082, 2001.

[23] E. de Miguel et al. *Molec. Phys.*, 72(3):593–605, 1991.

[24] E. de Miguel et al. *Molec. Phys.*, 74(2):405–424, 1991.

[25] D.C. Williamson, G. Jackson. *J. Chem. Phys.*, 108:10294, 1998.

[26] J. W. Perram et al. *Phys. Rev. E*, 54:6565, 1996.

[27] D.F. Rogers and J.A. Adams. *Mathematical elements for computer graphics, 2nd ed.* Mc Graw-Hill, 1990.

[28] W.H. Press, S.A. Teukolsky, W.T. Vetterling and B.P. Flannery. *Numerical recipes in C, the art of scientific computing.* Cambridge University Press, 1990.

[29] R. Berardi, S. Orlandi and C. Zannoni. *Phys. Rev. E*, in the press, 2003.

[30] D. Frenkel and B.M. Mulder. *Molec. Phys.*, 55:1171, 1985.

[000]	1.90456	[011]	0.51113	[101]	0.51113
[022]	2.01467	[202]	2.01467	[033]	-0.11376
[303]	-0.11376	[044]	0.91479	[404]	0.91479
[055]	-0.29937	[505]	-0.29937	[066]	0.41523
[606]	0.41523	[110]	-0.03942	[121]	-0.45400
[211]	-0.45400	[123]	0.59579	[213]	0.59579
[132]	0.17137	[312]	0.17137	[143]	-0.27083
[413]	-0.27083	[220]	-0.56137	[222]	-2.78379
[224]	2.41676	[231]	0.31104	[321]	0.31104
[233]	0.45382	[323]	0.45382	[242]	0.38115
[422]	0.38115	[244]	-1.69388	[424]	-1.69388
[246]	1.40664	[426]	1.40664	[330]	-0.07836
[440]	-0.17713	[442]	-0.52246		

Table 1: The non zero σ_{L_1,L_2,L_3} coefficients for the HP model and $k = 5$.

q	x	y
q_1	$-\frac{1}{2}\sigma_0$	0.0
q_2, q_3	0.0	$\frac{2}{3}k\sigma_0$
q_4	$\frac{1}{2}\sigma_0$	0.0
q_5	1.0	$-\frac{2}{3}k\sigma_0$
q_6	-1.0	$-\frac{2}{3}k\sigma_0$

Table 2: Coordinates for the pear shape Bezier points used for the PGHO model.

	$k = 3$	$k = 4$	$k = 5$
$a_{d,0}$	0.501852454	0.501377232	0.497721868
$a_{d,1}$	-0.141145314	-0.129608758	-0.123155821
$a_{d,2}$	-0.060542359	-0.074219217	0.024405876
$a_{d,3}$	0.225813650	0.484166441	0.723627215
$a_{d,4}$	0.832274021	0.923492941	0.389831429
$a_{d,5}$	-1.015039575	-1.987232902	-3.018638148
$a_{d,6}$	-2.504045172	-2.943008017	-1.951629076
$a_{d,7}$	1.375313426	2.808075172	4.413215403
$a_{d,8}$	3.196830129	3.815344782	2.998417509
$a_{d,9}$	-0.699241457	-1.426641750	-2.241573216
$a_{d,10}$	-1.430400139	-1.682476460	-1.416614353
$a_{l,0}$	1.498259615	1.995906501	2.493069403
$a_{l,1}$	-0.002027616	-0.004518187	-0.008067236

Table 3: Values of the $a_{d,\alpha}$ and $a_{l,\alpha}$ for the PHGO model with $k = 3$, 4 and 5
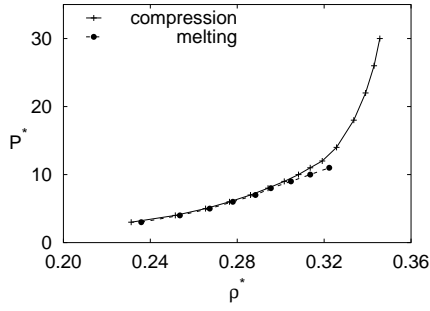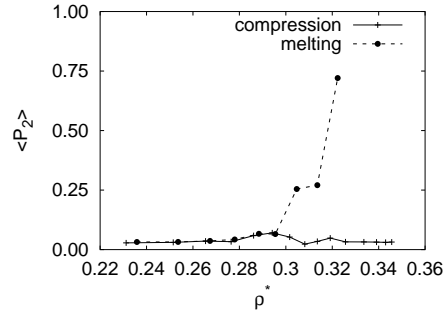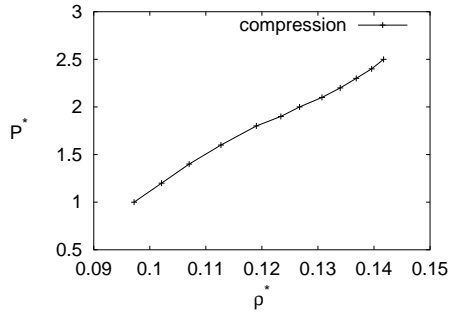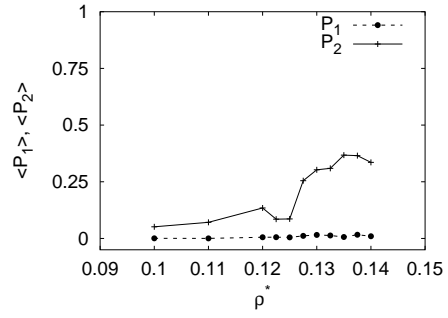
Figure 1: Results from constant NPT simulations of the truncated Stone expansion model obtained using $k = 3$(a,b) and $k = 5$(c,d). The curves for $k = 3$ and $k = 5$ correspond, respectively, to system sizes of $N = 1250$ and $N = 1000$.
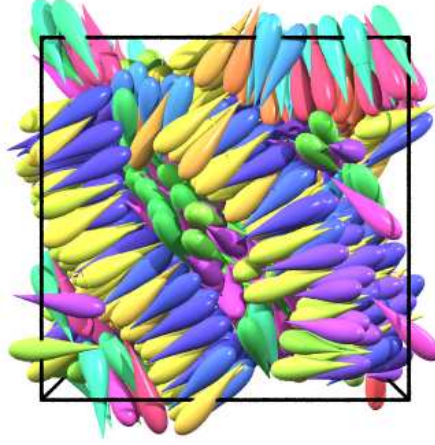
Figure 2: Configuration snapshot for the truncated Stone expansion model with $k = 5$ and $P^* = 2.5$.

(a) $k = 3$

(b) $k = 5$
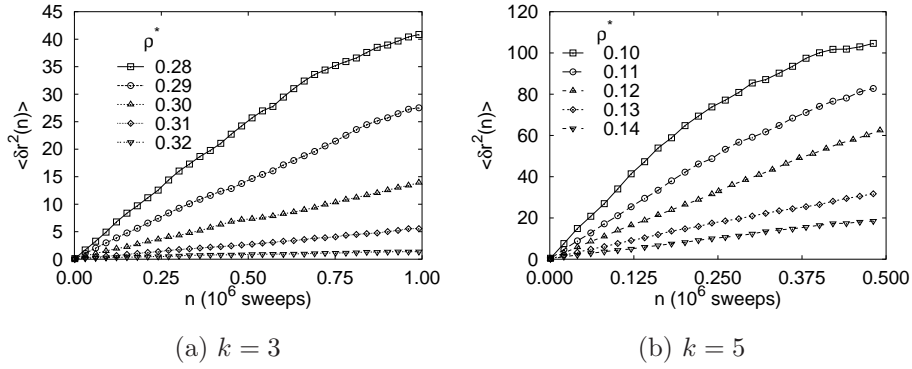
Figure 3: Particle mean square displacement curves obtained for the truncated Stone expansion model with $k = 3$ and $k = 5$. These data were obtained from constant NVT MC simulations. One sweep corresponds to N attempted Monte Carlo moves
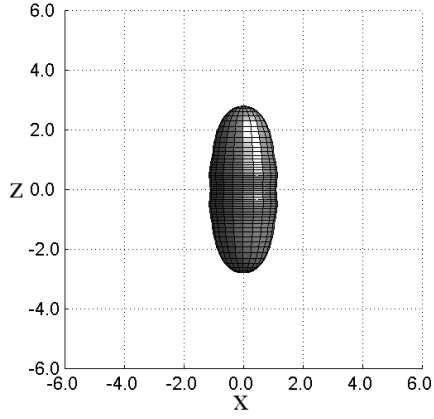
(a) Parallel particles.
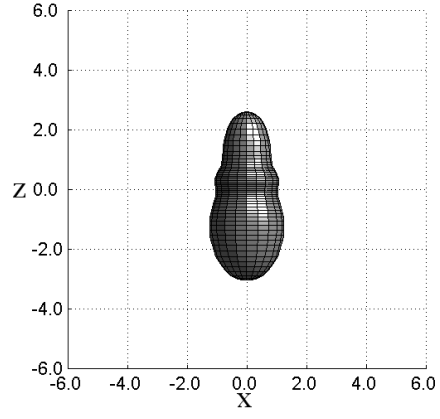
(b) Antiparallel particles.
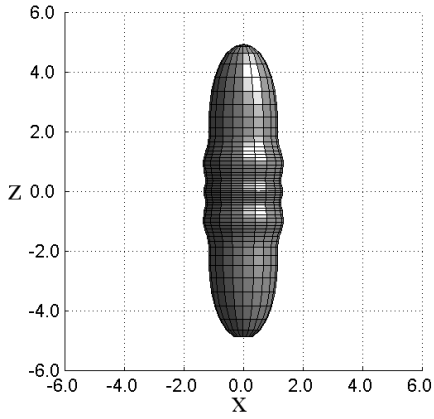
(c) Parallel particles.
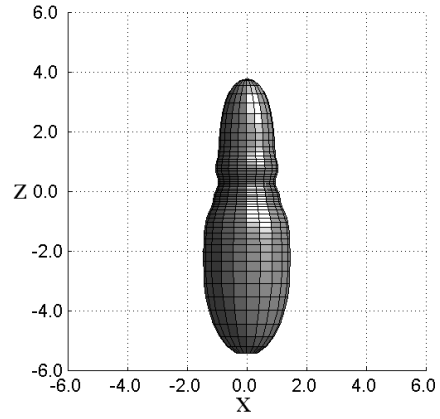
(d) AntiParallel particles.

Figure 4: Contact surfaces for the truncated Stone expansion model with $k = 3$(a,b) and $k = 5$(c,d).
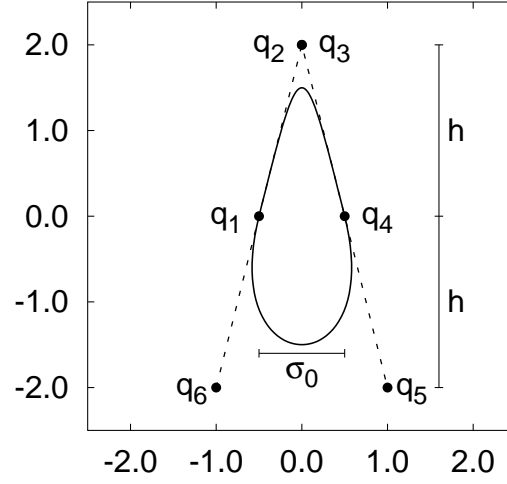
Figure 5: Bézier point geometry corresponding to the pear shape used for the PHGO model. For an elongation $k = 3$, $\sigma_0 = 1.0$ and $h = 2.0$.
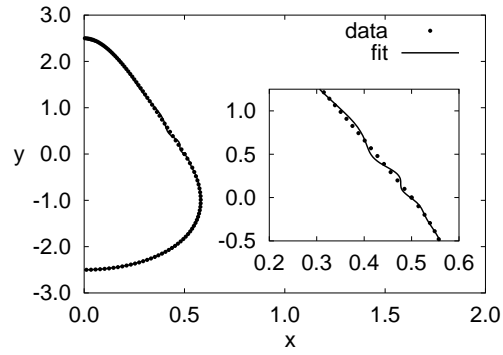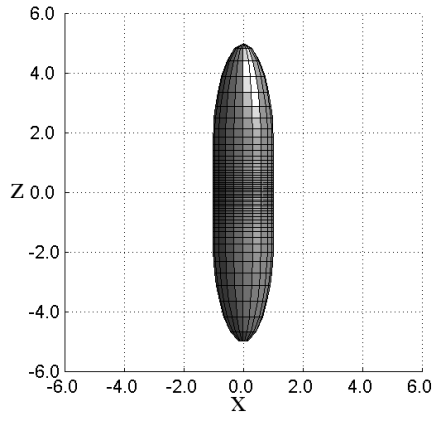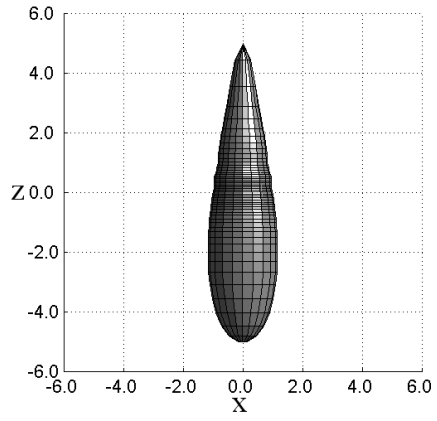

Figure 6: Fit of the PHGO model (line) to the Bézier curve (points) for k=5. Equivalent curves for $k = 3$ and 4 are similar but with better agreement.

(a) Parallel particles.   (b) Anti-parallel particles

Figure 7: Contact surfaces for the PHGO model with an elongation $k = 5$.
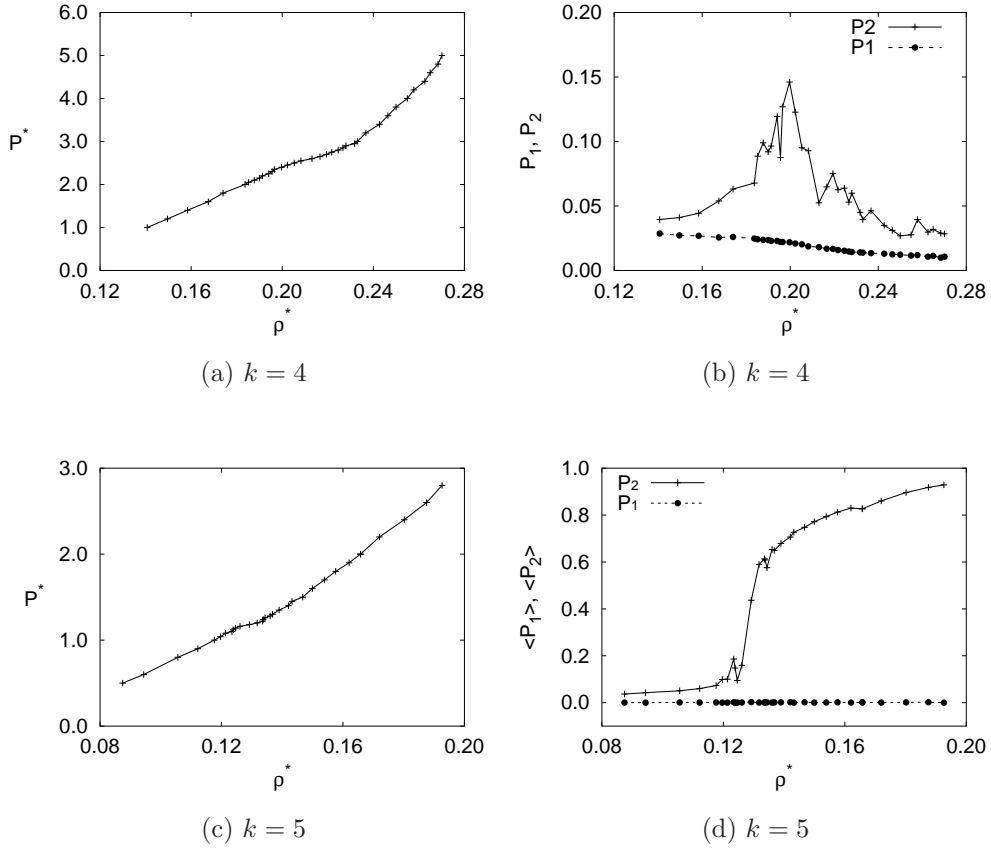For shorter elongations, the shapes are similar but smoother.

29

(a) $k = 4$

(b) $k = 4$

(c) $k = 5$

(d) $k = 5$

Figure 8: Results from constant NPT simulations of the PHGO model obtained with $k = 4$(a,b) and $k = 5$(c,d) and system sizes of $N = 1000$ particles.
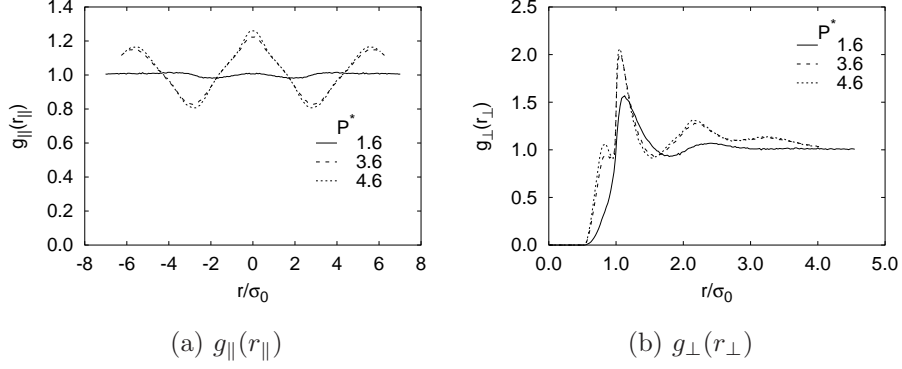
(a) $g_{\parallel}(r_{\parallel})$

(b) $g_{\perp}(r_{\perp})$

Figure 9: Pair correlation functions $g_{\perp}^{\mathrm{mol}}(r_{\perp})$ and $g_{\parallel}^{\mathrm{mol}}(r_{\parallel})$ resolved parallel and perpendicular to the molecular orientation for PHGO particles with elongation $k = 4$.

(a) $g_{\parallel}(r_{\parallel})$
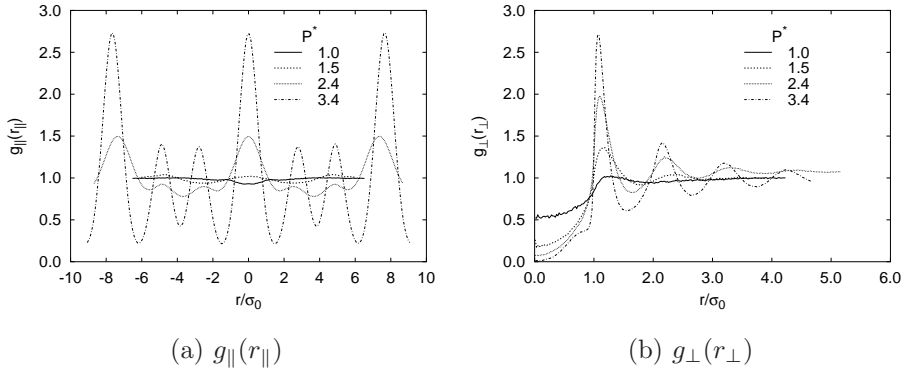
(b) $g_{\perp}(r_{\perp})$

Figure 10: Pair correlation functions $g_{\perp}(r_{\perp})$ and $g_{\parallel}(r_{\parallel})$ resolved parallel and perpendicular to the director for PHGO model particles with elongation $k = 5$.
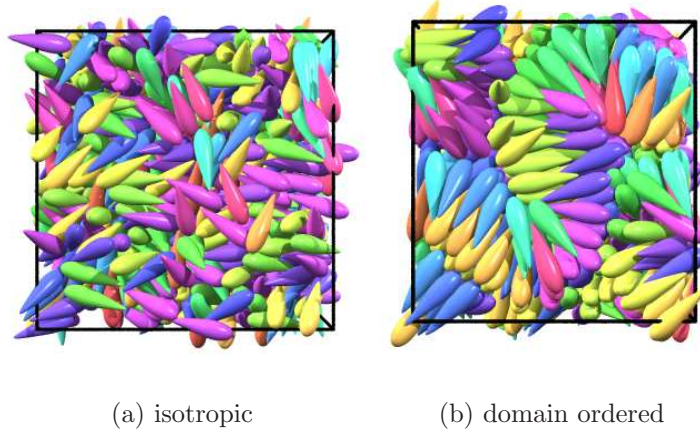
(a) isotropic   (b) domain ordered

Figure 11: Configuration snapshots of systems of $N = 1000$ PHGO particles with $k = 4$ at $P^* = 1.80$(a) and 5.00(b).

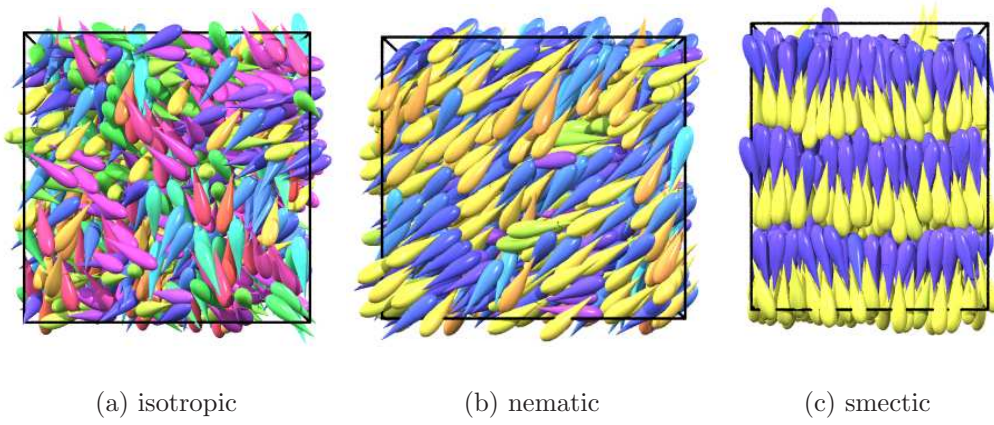(a) isotropic   (b) nematic   (c) smectic

Figure 12: Configuration snapshots of systems of $N = 1000$ PHGO particles with $k = 5$ and $P^* = 1.00$(a), 1.50(b) and 2.80(c).